

Interpretation of Disease Evidence for Medical Images Using Adversarial Deformation Fields

Ricardo Bigolin Lanfredi¹[0000-0001-8740-5796], Joyce D. Schroeder²[0000-0002-7451-4886], Clement Vachet¹[0000-0002-8771-1803], and Tolga Tasdizen¹[0000-0001-6574-0366]

¹ Scientific Computing and Imaging Institute,
University of Utah, Salt Lake City UT 84112, USA
`ricbl@sci.utah.edu`

² Department of Radiology and Imaging Sciences,
University of Utah, Salt Lake City UT 84112, USA

Abstract. The high complexity of deep learning models is associated with the difficulty of explaining what evidence they recognize as correlating with specific disease labels. This information is critical for building trust in models and finding their biases. Until now, automated deep learning visualization solutions have identified regions of images used by classifiers, but these solutions are too coarse, too noisy, or have a limited representation of the way images can change. We propose a novel method for formulating and presenting spatial explanations of disease evidence, called deformation field interpretation with generative adversarial networks (DeFI-GAN). An adversarially trained generator produces deformation fields that modify images of diseased patients to resemble images of healthy patients. We validate the method studying chronic obstructive pulmonary disease (COPD) evidence in chest x-rays (CXRs) and Alzheimer’s disease (AD) evidence in brain MRIs. When extracting disease evidence in longitudinal data, we show compelling results against a baseline producing difference maps. DeFI-GAN also highlights disease biomarkers not found by previous methods and potential biases that may help in investigations of the dataset and of the adopted learning methods.

Keywords: Deformation Field · Deep Learning Interpretation · Visual Attribution · Adversarial Training · Disease Effect · DeFI-GAN

1 Introduction

The recent surge of deep learning applications has the potential to revolutionize medical imaging in several ways, such as accessibility, efficiency, and flexibility. However, decision automation leads to challenges, including the interpretability of the outcomes [21]. Understanding what kinds of evidence deep learning methods capture from an image is one approach for overcoming these challenges.

Data used in preparation of this article were obtained from the Alzheimer’s Disease Neuroimaging Initiative (ADNI) database (adni.loni.usc.edu).

The field can benefit from such understanding through improvements in user trustworthiness, patient communication, and model bias identification.

Among visual attribution methods, backpropagation through a trained classifier is commonly used to determine areas of stronger influence on the model output [2]. Several visual attribution approaches have been applied to medical imaging. The class activation map (CAM) [37] method has been employed to show low-resolution areas of focus when performing pneumonia diagnosis from a chest x-ray (CXR) [27]. CAM has also been used as part of a weakly-supervised fine segmentation of lung nodules [10]. Layer-wise relevance propagation (LRP) [4] has been used to find biases in a histopathology dataset [17]. Despite their usefulness, most visual attribution methods are too coarse or too noisy for some applications [6]. They also have limited means of representing their findings, which may obscure relevant evidence.

Spatial deformations have been used in several applications, including registration [5], generation of adversarial examples [36], and creation of atlases [9]. While deformation fields may not be adequate for producing color and texture changes, they can generate variations in position, shape, and size. Since some impacts of diseases on anatomy are linked to the latter, we hypothesize that applying deformation fields to represent and visualize model interpretations will better include such variations. We propose the deformation field interpretation with generative adversarial networks (DeFI-GAN) method, which uses adversarial training [14] to learn to produce a deformation field that alters an image to make disease signs indiscernible. Therefore, the changes caused by this field express evidence of such disease. To the best of our knowledge, no other work has used deformation fields for visual attribution in deep learning.

We perform experiments studying evidence of chronic obstructive pulmonary disease (COPD) in CXRs [35, 13]. In [7], automatic assessment of COPD evidence is also performed. However, this assessment applies additive perturbations instead of deformation fields, and a different set of disease evidence is found. The method presented in [7] also models disease severity, which is not a focus of DeFI-GAN. We also employ the ADNI dataset to model the conversion from mild cognitive impairment (MCI) to Alzheimer’s disease (AD) through the morphological brain changes observed in MRIs [22]. In [6], generative adversarial training is also used to assess evidence of AD in brain MRIs. This setup inspires our method, but uses additive perturbations instead of deformation fields and a different regularization loss function. We analyze the outcomes of the proposed formulation in both datasets, showing that the use of DeFI-GAN improves longitudinal prediction over a baseline [6] and highlights additional disease evidence.

2 Method

We consider binary classification problems, where class 0 is associated with healthy patients and class 1 with diseased patients. Each image in a dataset is denoted by x , and its domain by X . Images of class c are indicated by x_c . Our objective is to find a transformation f that maps from an image x_1 containing

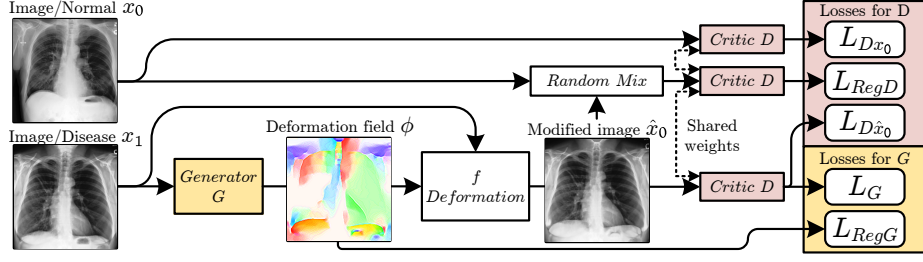


Fig. 1. Overall model architecture. The terms L_{Dx_0} , $L_{D\hat{x}_0}$, and L_G are WGAN losses, whereas L_{RegD} penalizes the gradient of D , and L_{RegG} penalizes the complexity of ϕ .

evidence for a disease to a modified image \hat{x}_0 where that evidence is absent. The rest of the content, e.g. patient specific anatomy, should not be modified. We propose to model f as a deformation controlled by a generated vector field, as shown in Figure 1. Mathematically,

$$\phi = G(x_1), \quad \hat{x}_0(p) = x_1(p + \phi(p)), \quad p \in X, \quad (1)$$

where G is a parameterized generator mapping from x_1 to vector field $\phi : X \rightarrow X$. Since $p + \phi(p)$ can lie between the set of coordinates on the grid for which we have defined values in x_1 , we use bilinear interpolation when $X \in \mathbb{R}^2$, and trilinear interpolation when $X \in \mathbb{R}^3$. When $p + \phi(p)$ lies outside the range for which values are defined in x_1 , values in \hat{x}_0 are set to 0.

To learn the parameters of transformation f , we follow [6] and use adversarial training. We train G jointly with a parameterized critic D tasked with discriminating modified images \hat{x}_0 from real images x_0 . The generator G is trained to fool D , using the gradient signal from D so that the distribution of \hat{x}_0 approaches the distribution of x_0 . For the adversarial loss, we use the WGAN [3] formulation. The critic D is trained to give high scores for modified images and low scores for real images, resulting in

$$L_D = L_{Dx_0} - L_{D\hat{x}_0} = \mathbb{E}[D(x_0)] - \mathbb{E}[D(\hat{x}_0)]. \quad (2)$$

To enforce the Lipschitz constraint required by the WGAN formulation [3], we use the penalty proposed in [15],

$$L_{RegD} = \mathbb{E} [(\|\nabla_{\tilde{x}} D(\tilde{x})\|_2 - 1)^2 \mid \tilde{x} \sim (1 - \alpha)x_0 + \alpha\hat{x}_0, \alpha \sim \mathcal{U}(0, 1)], \quad (3)$$

where $\mathcal{U}(0, 1)$ is the uniform distribution with support between 0 and 1. The expectation is approximated by sampling one α for each sampled (x_0, x_1) pair.

The generator G is trained to lower the scores for \hat{x}_0 , resulting in

$$L_G = \mathbb{E}[D(\hat{x}_0)]. \quad (4)$$

To penalize extraneous changes and enforce smooth and realistic deformations, we use a total variation denoising [29] penalty over ϕ . This term forces nearby

vectors to be aligned by penalizing $\int_X \|\nabla\phi\|_2$. After discretization,

$$L_{RegG} = \mathbb{E} \left[\frac{1}{P} \sum_{p \in X} \sum_{n \in \mathcal{N}(p)} \|\phi(p) - \phi(n)\|_2 \right], \quad (5)$$

where $\mathcal{N}(p)$ is the set of neighboring pixels of pixel p (4-neighborhood for $X \in \mathbb{R}^2$ and 6-neighborhood for $X \in \mathbb{R}^3$) and P is the total number of pixels.

The complete optimization formulation is given by

$$G^* = \underset{G}{\operatorname{argmin}}(L_G + \lambda_{RegG} L_{RegG}), D^* = \underset{D}{\operatorname{argmin}}(L_D + \lambda_{RegD} L_{RegD}), \quad (6)$$

where λ_{RegG} and λ_{RegD} are hyperparameters.

3 Experiments

We tested our method³ in two datasets, one for finding evidence of AD in brain MRIs and one for detecting signs of COPD in CXRs. We used as a baseline the visual attribution generative adversarial network (VA-GAN) method [6], where the function to obtain \hat{x}_0 is defined by the addition of a difference map, i.e., $\hat{x}_0 = x_1 + G(x_1)$, and the penalty on G is accordingly defined by $L_{RegG} = \|\hat{x}_0 - x_1\|_1$.

We used u-nets [28] as G 's architecture, varying the number of downsamplings and channels depending on the dataset. We used the Adam optimizer [20] with a learning rate of $1e-4$ and set $\lambda_{RegD} = 10$. For D 's architecture, we used an ImageNet pre-trained Resnet-18 [16] for the CXR dataset and a 10-layer network as in [6] for the MRI dataset. For training the DeFI-GAN method, we performed 100 updates to D for each update to G , whereas for VA-GAN, the 100:1 update ratio was used for the first 25 updates to G , and then changed to a 5:1 ratio. It was important for the convergence of G to have X represented in pixel units.

3.1 Chronic obstructive pulmonary disease in chest x-rays

We collected a dataset containing posterioranterior (PA) CXRs acquired at the University of Utah Hospital from 2012 to 2017. Each CXR was labeled for COPD using results from pulmonary function tests (PFTs) taken within one month of the CXR. Patients who received a lung transplant were excluded. Patients with COPD were assigned to class 1, and others were assigned to class 0. The training set was composed of patients who had only one CXR included in the dataset and contained 2,226 images from normal patients and 963 images from COPD patients. We worked under an approved Institutional Review Board (IRB)⁴ and anonymized data using Orthanc⁵. Image preprocessing included center-cropping to a square, resizing to 256×256 , cropping to 224×224 (randomly for training and centered for validation and testing), and equalizing histograms.

³ The DeFI-GAN code is available at <https://github.com/ricbl/defigan>

⁴ IRB_00104019, PI: Schroeder MD

⁵ orthanc-server.com

3.2 Alzheimer’s disease in brain MRIs

The ADNI dataset was collected to characterize the progression of AD and contains brain MRIs of thousands of subjects followed for a few years [1]. Diagnosis of AD and MCI are provided for each exam. Following [6], we set class 0 to MCI patients, instead of healthy patients, and class 1 to AD patients, training G to provide interpretations for the conversion from MCI to AD. We also limited our study to T1-weighted MRIs from the ADNI1, ADNIGO, and ADNI2 cohorts.

Data splits and part of the preprocessing were replicated from [6]⁶. For each image, we used the FMRIB Software Library (FSL) toolbox [32] v6.0 for reorientation and field of view (FOV) cropping, N4 Bias Correction [34] from Advanced Normalization Tools (ANTs) v3.0 for bias field correction, FSL to register the image to the MNI 152 space [11, 12], and ROBEX [18] v1.2 for skull stripping. To correct cases where ROBEX failed, we added another step of skull stripping to the whole dataset using the Brain Extraction Tool (BET) [31] with a fractional intensity threshold equal to 0.25. All volumes were rescaled to a size of $128 \times 160 \times 112$ pixels. Through visual inspection, we searched for cases where the brain volume was incorrectly oriented, or skull stripping had failed, and removed 7 volumes from 4 subjects from test and validation. The preprocessing differed from [6] in the application of BET and in the elimination of the 7 cases for which preprocessing failed. The final training set had 2,528 MCI volumes and 1,198 AD volumes, for a total of 825 subjects.

3.3 Quantitative Validation

We validated our generated disease evidence by using longitudinal scans demonstrating disease progression. For the COPD dataset, we paired all test cases where a subject was healthy in the baseline CXR with cases of the same subject after developing COPD. For each pair, we performed an affine registration of the normal case to the COPD case using SimpleITK v1.2 [24]. We then subtracted the COPD image from the registered baseline image to get a difference ground truth Δx . The final split sizes were 206 pairs of images (176 subjects) for validation and 547 pairs (354 subjects) for testing. For the ADNI dataset, we performed rigid registration instead of affine, disregarding the background for the calculations, and used MCI cases as the baseline, pairing them with AD MRIs taken with the same field strength. The final split sizes were 207 pairs (102 subjects) for validation and 259 pairs (143 subjects) for testing.

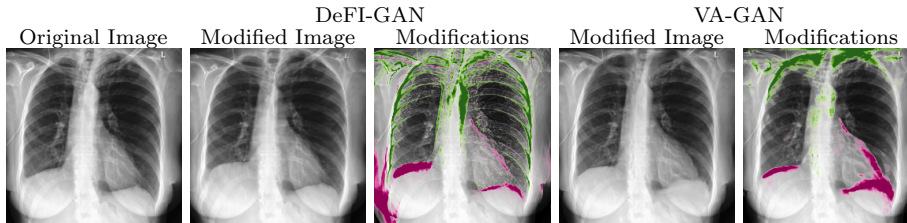
The ground truth Δx and the predicted difference $\widehat{\Delta x} = \hat{x}_0 - x_1$ were compared using normalized cross-correlation (NCC), masked to ignore regions padded during registration and skull stripping. This operation was defined by

$$\text{NCC}(\Delta x, \widehat{\Delta x}) = \frac{1}{M-1} \sum_{p \in \mathcal{M}} \frac{(\Delta x(p) - \mu_{\Delta x})}{\sigma_{\Delta x}} \times \frac{(\widehat{\Delta x}(p) - \mu_{\widehat{\Delta x}})}{\sigma_{\widehat{\Delta x}}}, \quad (7)$$

⁶ VA-GAN’s original preprocessing code, list of subjects, and TensorFlow implementation are available in <https://github.com/baumgach/vagan-code/>

Table 1. NCC scores for the compared methods. Averages of 5 models trained with different random seeds are reported with their standard deviations.

Dataset\Method	VA-GAN	DeFI-GAN
ADNI	0.332 ± 0.015	0.365 ± 0.014
COPD	0.174 ± 0.007	0.204 ± 0.006

**Fig. 2.** Comparison of results of DeFI-GAN and VA-GAN on the COPD dataset. Green represents darkening of the image, and pink represents brightening.

where M is the number of pixels in the mask \mathcal{M} , and μ_i and σ_i are, respectively, the average value and the unbiased standard deviation of values of pixels of image i inside mask \mathcal{M} . One subject may have had more than one pair of validation images. The score calculated for all pairs of each subject was averaged before calculating the final average score to avoid the over-representation of a few subjects in the final score.

Hyperparameters were chosen by considering image quality and validation NCC score. With the DeFI-GAN method, we used $\lambda_{RegG} = 25$ for the COPD dataset and $\lambda_{RegG} = 10$ for the ADNI dataset, whereas for the VA-GAN method we used, respectively, $\lambda_{RegG} = 50$ and $\lambda_{RegG} = 100$. The original VA-GAN TensorFlow implementation was used for the ADNI dataset.

Test scores are reported in Table 1, where the DeFI-GAN method is shown to outperform the baseline. The scores for the ADNI dataset when using VA-GAN are better than the ones presented in [6]. This difference is probably due to choosing the best training epoch using the NCC validation score instead of loss values. It is interesting to note that training was less noisy for the DeFI-GAN method when considering the validation scores from epoch to epoch. Relatively low NCC scores may result from the difficulty in aligning longitudinal data and from aging effects in the ground truth.

3.4 Biomarker Validation

We compared the interpretations provided by DeFI-GAN and VA-GAN and present some results in Figures 2 and 3. The difference maps were computed using $\hat{x}_0 - x_1$. Additional results are presented in the supplementary material. For the COPD dataset, both approaches identified changes in heart silhouette

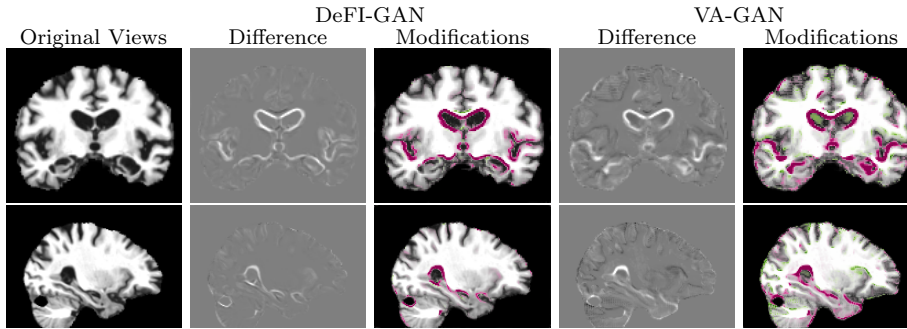


Fig. 3. Results on the ADNI dataset when removing evidence of AD from the original image. Green represents darkening of the image, and pink represents brightening.

and in diaphragm height and curvature, which are notable characterizations of COPD in CXRs [35, 13]. We found no variation in lung lucency. The lack of change in texture was expected for the DeFI-GAN method from its formulation. Interpretations from the VA-GAN method were less spatially smooth.

Saber-sheath trachea is a secondary sign of COPD, and, when it occurs, there is a narrowing of the trachea in the frontal CXR [8]. This evidence was more identifiable in models trained with DeFI-GAN when looking at quiver plot visualization, as seen in Figure 4(a). The VA-GAN method cannot produce this kind of deformation field visualization. In the difference map produced by the VA-GAN method, the changes in the top of the image appeared as a dark fuzzy alteration. Another sign more easily identified with DeFI-GAN was the change in soft-tissue thickness, as shown in Figure 4(b). This change is in accordance with the correlation between low body mass index (BMI) and COPD [38].

Although we focused the analysis on COPD, we also found the results in the ADNI dataset consistent with the literature. The main changes associated with AD, expansion of ventricles, hippocampus atrophy, and temporal lobe atrophy [22], are seen in Figure 3. It was possible to find, in some cases, atrophies in the precuneus, the cerebellum, and the brainstem. These regions have been associated with AD [30, 33, 23]. The rest of the cortex also presented atrophies to a lesser extent. The differences highlighted by both methods were similar, except for VA-GAN having more image noise, more darkening differences, and more noticeable highlighting of the hippocampus, which is favorable evidence. A detailed representation of a deformation field in MRIs can be seen in the supplementary material.

Unexpected changes in COPD Some evidence pinpointed by the DeFI-GAN method in the COPD dataset is not usually listed in the literature. Figure 4(c) shows a decrease in gastric bubble size. This change may represent a confusion between the lower border of the gastric bubbles and the diaphragm, or be related to aerophagia due to coughing [25]. Furthermore, the shoulder position changed

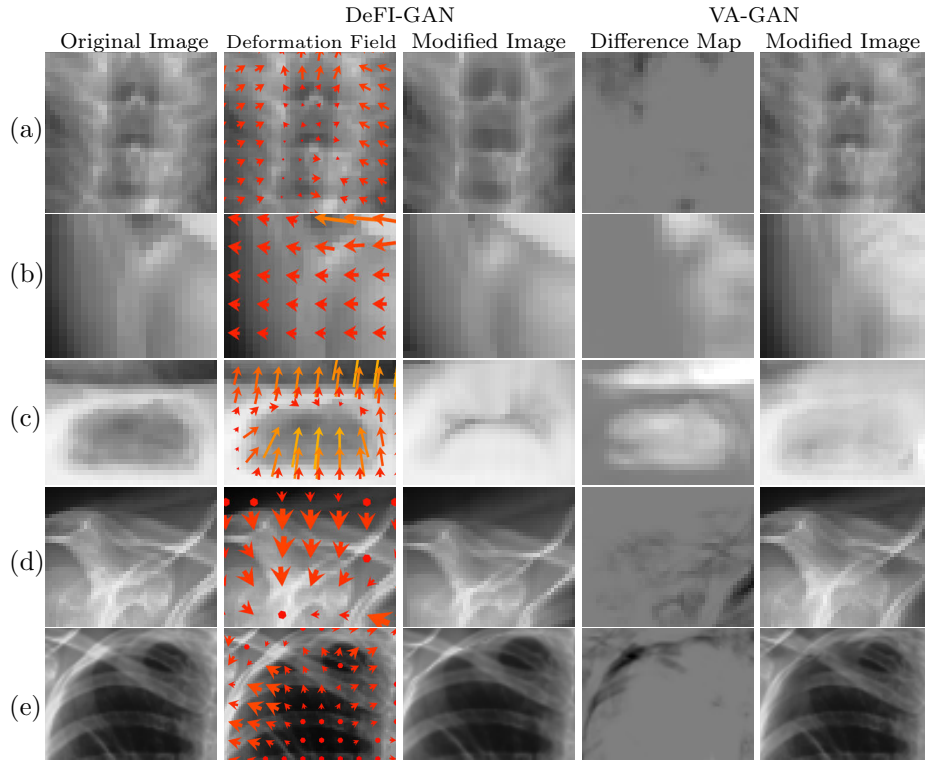


Fig. 4. Details on the generated deformation fields and comparison with VA-GAN. The color of the arrows represents their length. For rows **a-c**, their length represents the exact shift in pixels. In rows **d-e**, their length is multiplied by 2 for better visualization. The full-size images are presented in the supplementary material. From top to bottom: **(a)** trachea; **(b)** soft tissue; **(c)** gastric bubble; **(d)** shoulder; **(e)** lung apex.

in a few images, as seen in Figure 4(d). High clavicle position might be related to a decrease in shoulder mobility [26] and, consequently, difficulty in following the required body positioning for the standing CXR acquisition. It may also be related to a bias in spine position due to the prevalence of osteoporosis [19] in patients with COPD. In Figure 4(e), the expansion of the top of the lungs contradicts larger lung volumes in COPD patients. However, when analyzed by a radiologist, lung volume still seemed larger in the original images, probably due to diaphragm height. This change may be correlated with the clavicle positioning since it increases lung volume above the clavicle. The change in gastric bubble size and the expansion of the top of the lung were, in a less comprehensible representation, also highlighted by the VA-GAN method. All these unexpected differences may also represent dataset biases. A more in-depth investigation of the causes for these changes is left to subsequent studies.

4 Conclusion

We formulated a method for producing interpretations of the disease evidence that deep learning models can capture from imaging data, using deformation fields and adversarial training. This method performed better in the proposed longitudinal quantitative validation on two medical datasets, when compared to another method with a similar goal. Furthermore, it allowed for easier discovery of qualitative disease evidence used by the model. As exemplified by some of the highlighted COPD evidence, this study has the potential to support future analyses of unexpected biases in medical imaging datasets.

References

1. About ADNI (2017), <http://adni.loni.usc.edu/about/>, accessed on 2020-03-11
2. Ancona, M., Ceolini, E., Öztireli, C., Gross, M.: Towards better understanding of gradient-based attribution methods for deep neural networks. In: ICLR (2018)
3. Arjovsky, M., Chintala, S., Bottou, L.: Wasserstein generative adversarial networks. In: ICML (2017)
4. Bach, S., Binder, A., Montavon, G., Klauschen, F., Müller, K.R., Samek, W.: On pixel-wise explanations for non-linear classifier decisions by layer-wise relevance propagation. PLOS ONE **10**(7), 1–46 (2015). <https://doi.org/10.1371/journal.pone.0130140>
5. Balakrishnan, G., Zhao, A., Sabuncu, M.R., Guttag, J., Dalca, A.V.: An unsupervised learning model for deformable medical image registration. In: CVPR (2018)
6. Baumgartner, C.F., Koch, L.M., Tezcan, K.C., Ang, J.X.: Visual feature attribution using Wasserstein GANs. In: CVPR (2018). <https://doi.org/10.1109/CVPR.2018.00867>
7. Bigolin Lanfredi, R., Schroeder, J.D., Vachet, C., Tasdizen, T.: Adversarial regression training for visualizing the progression of chronic obstructive pulmonary disease with chest x-rays. In: MICCAI (2019). https://doi.org/10.1007/978-3-030-32226-7_76
8. Ciccacese, F., et al.: Saber-sheath trachea as a marker of severe airflow obstruction in chronic obstructive pulmonary disease. *La radiologia medica* **119**(2), 90–96 (2014). <https://doi.org/10.1007/s11547-013-0318-3>
9. Dalca, A., Rakic, M., Guttag, J., Sabuncu, M.: Learning conditional deformable templates with convolutional networks. In: NeurIPS (2019)
10. Feng, X., Yang, J., Laine, A.F., Angelini, E.D.: Discriminative localization in CNNs for weakly-supervised segmentation of pulmonary nodules. In: MICCAI (2017). https://doi.org/10.1007/978-3-319-66179-7_65
11. Fonov, V., Evans, A.C., Botteron, K., Almli, C.R., McKinstry, R.C., Collins, D.L.: Unbiased average age-appropriate atlases for pediatric studies. *NeuroImage* **54**(1), 313 – 327 (2011). <https://doi.org/10.1016/j.neuroimage.2010.07.033>
12. Fonov, V., Evans, A., McKinstry, R., Almli, C., Collins, D.: Unbiased nonlinear average age-appropriate brain templates from birth to adulthood. *NeuroImage* **47**, S102 (2009). [https://doi.org/10.1016/S1053-8119\(09\)70884-5](https://doi.org/10.1016/S1053-8119(09)70884-5)
13. Foster, W.L., et al.: The emphysemas: radiologic-pathologic correlations. *RadioGraphics* **13**(2), 311–328 (1993). <https://doi.org/10.1148/radiographics.13.2.8460222>

14. Goodfellow, I., et al.: Generative adversarial nets. In: NeurIPS (2014)
15. Gulrajani, I., Ahmed, F., Arjovsky, M., Dumoulin, V., Courville, A.: Improved training of Wasserstein GANs. In: NeurIPS (2017)
16. He, K., Zhang, X., Ren, S., Sun, J.: Deep residual learning for image recognition. In: CVPR (2016). <https://doi.org/10.1109/CVPR.2016.90>
17. Hägele, M., et al.: Resolving challenges in deep learning-based analyses of histopathological images using explanation methods. CoRR **abs/1908.06943** (2019)
18. Iglesias, J.E., Liu, C., Thompson, P.M., Tu, Z.: Robust brain extraction across datasets and comparison with publicly available methods. IEEE Trans. Med. Imag. **30**(9), 1617–1634 (2011). <https://doi.org/10.1109/TMI.2011.2138152>
19. Jaramillo, J.D., et al.: Reduced bone density and vertebral fractures in smokers. Men and COPD patients at increased risk. Ann. Am. Thorac. Soc. **12**(5), 648–656 (2015). <https://doi.org/10.1513/AnnalsATS.201412-591OC>
20. Kingma, D.P., Ba, J.: Adam: A method for stochastic optimization. In: ICLR (2015)
21. Langlotz, C.P., et al.: A roadmap for foundational research on artificial intelligence in medical imaging: From the 2018 NIH/RSNA/ACR/the academy workshop. Radiology **291**, 781–791 (2019)
22. Ledig, C., Schuh, A., Guerrero, R., Heckemann, R., Rueckert, D.: Structural brain imaging in Alzheimer’s disease and mild cognitive impairment: biomarker analysis and shared morphometry database. Scientific Reports **8** (2018). <https://doi.org/10.1038/s41598-018-29295-9>
23. Lee, J., Ryan, J., Andreescu, C., Aizenstein, H., Lim, H.K.: Brainstem morphological changes in Alzheimer’s disease. Neuroreport **26**, 411–415 (05 2015). <https://doi.org/10.1097/WNR.0000000000000362>
24. Lowekamp, B., Chen, D., Ibanez, L., Blezek, D.: The design of SimpleITK. Frontiers in Neuroinformatics **7**, 45 (2013). <https://doi.org/10.3389/fninf.2013.00045>
25. Martin-Harris, B.: Optimal patterns of care in patients with chronic obstructive pulmonary disease. In: Seminars in speech and language. vol. 21(04), pp. 0311–0322 (2000). <https://doi.org/10.1055/s-2000-8384>
26. Morais, N., Cruz, J., Marques, A.: Posture and mobility of the upper body quadrant and pulmonary function in COPD: an exploratory study. Brazilian Journal of Physical Therapy **20**, 345 – 354 (2016). <https://doi.org/10.1590/bjpt-rbf.2014.0162>
27. Rajpurkar, P., Irvin, J., et al.: Chexnet: Radiologist-level pneumonia detection on chest x-rays with deep learning. CoRR **abs/1711.05225** (2017)
28. Ronneberger, O., Fischer, P., Brox, T.: U-net: Convolutional networks for biomedical image segmentation. In: MICCAI (2015). https://doi.org/10.1007/978-3-319-24574-4_28
29. Rudin, L.I., Osher, S., Fatemi, E.: Nonlinear total variation based noise removal algorithms. Physica D: Nonlinear Phenomena **60**(1), 259 – 268 (1992). [https://doi.org/10.1016/0167-2789\(92\)90242-F](https://doi.org/10.1016/0167-2789(92)90242-F)
30. Scahill, R.I., Schott, J.M., Stevens, J.M., Rossor, M.N., Fox, N.C.: Mapping the evolution of regional atrophy in Alzheimer’s disease: Unbiased analysis of fluid-registered serial MRI. PNAS **99**(7), 4703–4707 (2002). <https://doi.org/10.1073/pnas.052587399>
31. Smith, S.M.: Fast robust automated brain extraction. Hum Brain Mapp **17**(3), 143–155 (2002). <https://doi.org/10.1002/hbm.10062>
32. Smith, S.M., et al.: Advances in functional and structural MR image analysis and implementation as FSL. NeuroImage **23**, S208 – S219 (2004). <https://doi.org/10.1016/j.neuroimage.2004.07.051>

33. Tabatabaei Jafari, H., Walsh, E., Shaw, M., Cherbuin, N.: The cerebellum shrinks faster than normal ageing in Alzheimer’s disease but not in mild cognitive impairment. *Hum Brain Mapp* **38** (03 2017). <https://doi.org/10.1002/hbm.23580>
34. Tustison, N.J., et al.: N4ITK: Improved N3 bias correction. *IEEE Trans. Med. Imag.* **29**(6), 1310–1320 (2010). <https://doi.org/10.1109/TMI.2010.2046908>
35. Washko, G.R.: Diagnostic imaging in COPD. In: *Semin Resp Crit Care*. vol. 31(3), pp. 276–285 (2010). <https://doi.org/10.1055/s-0030-1254068>
36. Xiao, C., Zhu, J.Y., Li, B., He, W., Liu, M., Song, D.: Spatially transformed adversarial examples. In: *ICLR* (2018)
37. Zhou, B., Khosla, A., Lapedriza, A., Oliva, A., Torralba, A.: Learning deep features for discriminative localization. In: *CVPR* (2016). <https://doi.org/10.1109/CVPR.2016.319>
38. Zhou, Y., et al.: The association between BMI and COPD: The results of two population-based studies in Guangzhou, China. *COPD* **10**(5), 567–572 (2013). <https://doi.org/10.3109/15412555.2013.781579>

Supplementary Material



Fig. 1. Deformation field for an ADNI image. Arrow length is multiplied by 5.

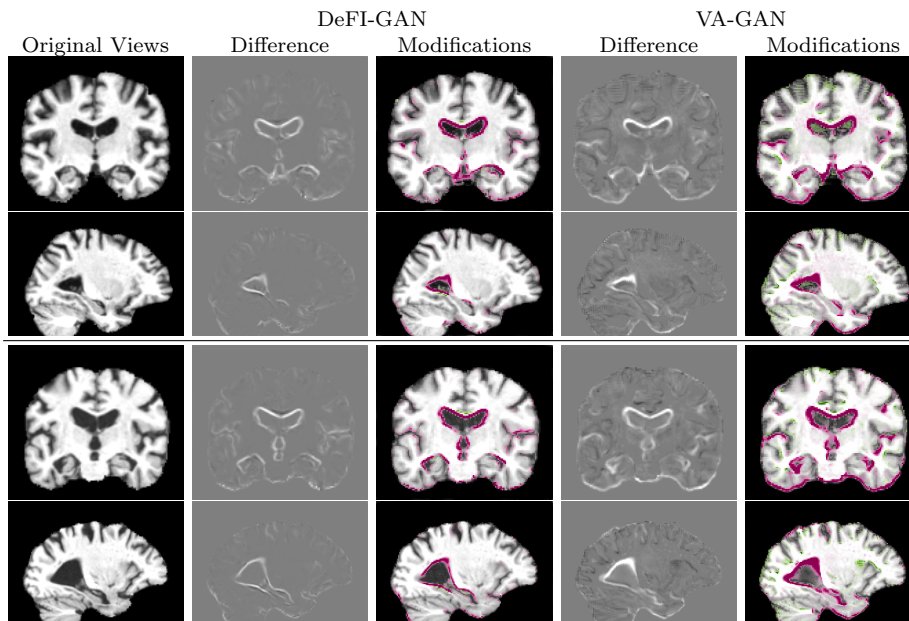


Fig. 2. Additional results for the ADNI dataset.

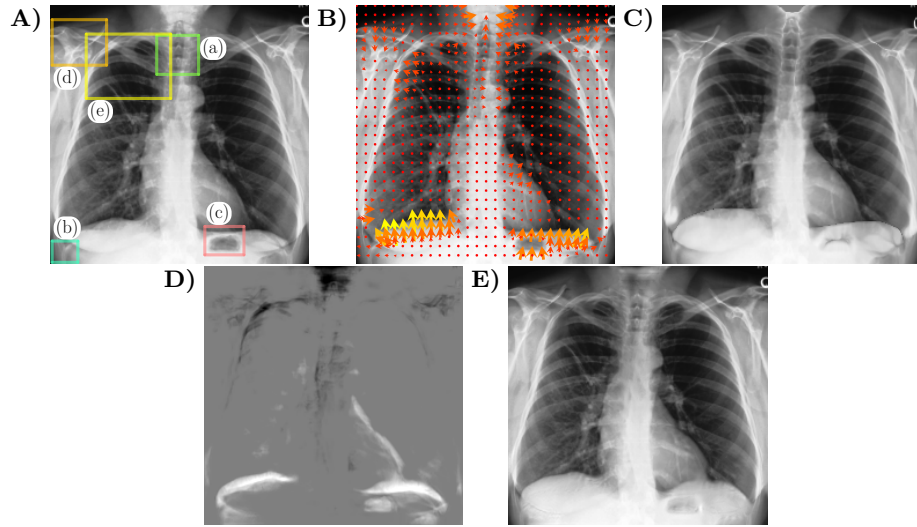


Fig. 3. Full-size images of the portions used in Figure 4 in the main paper: **A)** cropped regions labeled by their row labels over the original image; **B)** deformation field with arrow length scaled by 2; **C)** image modified by DeFI-GAN; **D)** VA-GAN difference map; **E)** image modified by VA-GAN.

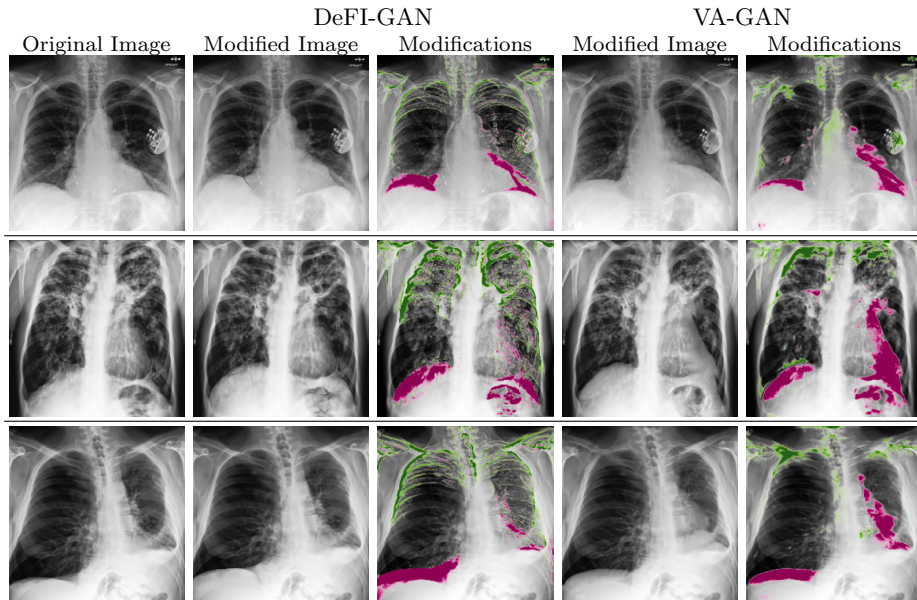


Fig. 4. Additional results for the COPD dataset.